PHOTONICS Research

Strong coupling of excitons with transverse-electric-polarized polaritons for high-precision MoS$_2$ layer number sensing in Au/MoS$_2$ heterostructures

Leyang Li,[1] Yunbao Zheng,[2] Min Ouyang,[1] Haihua Fan,[1] Qiaofeng Dai,[1] Haiying Liu,[1,*] Lijun Wu,[1] and Sheng Lan[1]

[1]*Guangdong Basic Research Center of Excellence for Structure and Fundamental Interactions of Matter, Guangdong Provincial Key Laboratory of Nanophotonic Functional Materials and Devices, School of Optoelectronic Science and Engineering, South China Normal University, Guangzhou 510665, China*
[2]*School of Optoelectronic Engineering, Guangdong Polytechnic Normal University, Guangzhou 510665, China*
**Corresponding author: hyliu@scnu.edu.cn*

Received 6 May 2025; revised 1 July 2025; accepted 15 July 2025; posted 21 July 2025 (Doc. ID 566250); published 1 October 2025

Surface plasmon polaritons (SPPs) on metal surfaces excited by p-polarized light have long been a crucial method for achieving light–matter interactions due to their small mode-field volumes and strong optical localization properties. However, the significant losses generated in metals greatly limit the intensity of the SPPs and their potential application scenarios. In this paper, we leverage the high refractive index properties of two-dimensional (2D) transition metal dichalcogenides (TMDCs) to generate transverse-electric (TE) polarized waves excited by s-polarized light on the surface of gold nanofilms by accurately controlling the number of the TMDC layers and the spatial refractive index variations with the structure. Unlike the SPPs excited by p-polarized light, the TE surface waves on the surface of the gold film exhibit low loss and high quality factor (*Q* factor). Moreover, the difference in refractive index causes the TE surface waves to be electromagnetically separated in space, lifting the electric field component in the excited TE surface waves from the surface of the metal film into the TMDCs, thereby minimizing the ohmic loss in the metal and enabling strong coupling between the TE surface waves and the two-exciton states (A-exciton and B-exciton) in the TMDCs. Experimental results demonstrated the strong coupling of TE waves with double excitons (A-exciton and B-exciton) in multilayer MoS$_2$ by exciting the Au/MoS$_2$ heterostructure using a Kretschmann–Raether configuration, showing ultrahigh Rabi splitting up to about 310 meV. Furthermore, the number of MoS$_2$ layers can be accurately determined by measuring the redshift of the Rabi splitting peak of the strong coupling spectra in the Au/MoS$_2$ heterostructure. Our findings open a new avenue for manipulating strong exciton–photon coupling in 2D materials and offer a novel approach for accurately characterizing the thickness of TMDCs.

https://doi.org/10.1364/PRJ.566250

1. INTRODUCTION

The interaction between light and matter has been a prominent research topic in the field of modern optics. It is well established that when the rate of energy exchange between photons and excitons exceeds the average damping rate between them [1–4], the photons and excitons will be superimposed to form a hybrid state with part-light and part-matter characteristics [5,6], also known as an exciton polariton. This process, also referred to as the exciton–photon strong coupling process, is evidenced by the presence of Rabi splitting in the spectrum [7–11]. Exciton–photon strong coupling has important applications in ultrafast optical switching [12–14], low-threshold semiconductor lasers [15–17], and quantum manipulation [18,19].

In recent years, transition metal dichalcogenides (TMDCs) have emerged as a significant platform for investigating light–matter interactions [20–23]. TMDCs have a variety of excitonic states with large binding energies and dipole moments at room temperature [24–26], which provides ideal conditions for studying exciton–photon strong coupling. MoS$_2$ and WS$_2$ are two commonly used materials for achieving strong exciton–photon coupling in TMDCs. Both materials exhibit two stable existing exciton resonances in the visible spectral range, known as A-exciton and B-exciton (X_A and X_B), respectively [27–30].

In most cases, only the strong coupling occurring in the A-exciton is observed, since the dipole moment of the B-exciton is much smaller compared to the A-exciton. As the thickness of the TMDC gradually increases, the number of excitons involved in the coupling also increases. This allows for the observation of B-exciton involvement in the strong coupling process. Plasma–exciton strong coupling in multilayer MoS_2 has been investigated [31], and reports on strong coupling in multilayer TMDCs have been gradually increasing in recent years [32–38]. When the TMDCs increase from a monolayer to a multilayer, they undergo a shift from a direct bandgap material to an indirect bandgap material. This change significantly impacts the photoluminescence (PL) and exciton response of the TMDCs [39–45]. At the same time, the number of layers of TMDCs will further affect its valley-selective properties [46–51] and nonlinear optical response [52–55]. Therefore, accurate characterization of TMDCs layers is crucial in understanding light–matter interaction.

Taking advantage of the high refractive index of monolayer TMDCs, the multibeam interference effect causes multilayer TMDCs with varying thicknesses to exhibit different colors under the microscope [38,56,57]. This color variation enables rapid determination of the number of layers in TMDCs. However, this method can only give an estimated range of the number of layers of TMDCs, which should only be considered an indicative rather than an accurate means of thickness characterization. Alternatively, the number of TMDCs layers can be determined by Raman spectroscopy. However, this method is typically applicable for determining the layer number of monolayer to few-layer TMDCs. For TMDCs with a thickness exceeding 10 nm, Raman spectroscopy shifts are not easily discernible [58,59]. Currently, the principal nonoptical methodology for quantifying the number of layers in the TMDCs continues to rely on atomic force microscopy (AFM) or the observation of scanning electron microscopy (SEM) images of cross sections of the TMDCs. However, it is important to note that all of the aforementioned methods have the potential to inflict varying degrees of damage upon the two-dimensional (2D) material itself, which could ultimately compromise its structural integrity.

It has been demonstrated that the exciton–plasma strong coupling can be achieved by using surface plasmon polaritons (SPPs) supported in metal films [60,61]. Compared to metal nanoparticles or nanostructures, SPPs supported on the surface of the metal films have more open geometrical surfaces, making it easier to introduce excitonic materials and manipulate strong coupling. However, the ohmic losses generated during the propagation of SPPs in metals significantly reduce the quality factor (Q factor) and coupling strength of the strong coupling system, severely limiting its application in practical optical devices. SPPs supported on the surface of a metal film can only be excited by p-polarized transverse magnetic (TM) light, as s-polarized transverse electric (TE) light cannot induce the collective oscillation of electrons on the metal surface. However, TE waves can propagate on a metal surface when it is coated with a dielectric layer of sufficient thickness [62]. For instance, low-order TE modes have been achieved by covering Ag thin films with a Si_3N_4 layer of a certain thickness [63]. Additionally, covering the Ag/Si_3N_4 heterostructure with TMDCs enables the strong coupling of single exciton. Nevertheless, the TE wave generated in this manner primarily propagates along the surface propagation of the dielectric layer, with only a portion of the electric field localized in the 2D material, leading to losses that severely restrict the range of TMDC thickness in the strong coupling, while the weak electric field localization effect significantly reduces the coupling strength. Furthermore, the presence of the dielectric layer complicates the subsequent regulation of strong coupling device based on the TMDCs.

In this paper, we utilize Au/MoS_2 heterostructures composed of Au nanofilms and multilayered MoS_2 to realize TE polarized waves that propagate stably in the visible light range excited by *s*-polarized light. By accurately controlling the dimensions of the TMDCs and the thickness of the Au nanofilms, stable TE wave propagation is achieved. The high refractive index of the TMDCs (around 4.5 for MoS_2), allows the TE wave propagation to be realized directly in the Au/MoS_2 heterostructure provided the thickness of the modulated 2D material exceeds the critical thickness threshold, thus obviating the need for a dielectric layer on the metal surface. This configuration results in very low losses and high Q factor up to 42.9 in the Au/MoS_2 heterostructure, with the electric field component of the spatial electromagnetic separation being almost entirely localized in the MoS_2, significantly enhancing the system's coupling strength. Consequently, the TE wave strongly couples with the MoS_2 double excitons (A-exciton and B-exciton), allowing for tuning of the photon–exciton detuning in the strong coupling system by varying the incident light angle and adjusting the MoS_2 thickness. Experimentally, it is demonstrated that the Kretschmann–Raether (K–R) device can be used to excite Au/MoS_2 heterostructures and extract strong coupling information. Using polystyrene (PS) nanospheres with broad lines in the visible spectrum as scattering antennas, an ultrahigh Rabi splitting of 310 meV is measured in the strong coupling scattering spectrum. Furthermore, by preparing different Au/MoS_2 heterostructures with MoS_2 layers ranging from 33 to 39 (thicknesses corresponding to 20.2 to 25.1 nm), we observe a clear redshift in the Rabi splitting peak as the number of MoS_2 layers increases. The change in the number of MoS_2 layers and the shift in the strong coupling spectrum follow a certain linear relationship, with spectral redshift enabling accurate and nondestructive sensing of the MoS_2 layer number through the strong coupling of TE waves to MoS_2 excitons.

2. RESULTS AND DISCUSSION

A. Theoretical Analysis and Numerical Simulation of TE-Polarized Wave

In Fig. 1(a), we show the heterostructure consisting of a 50 nm Au film deposited on a SiO_2 substrate and multilayers of MoS_2 covering the Au film. In Fig. 1(b), we show schematically that the excited TE wave propagates in MoS_2 and produces strong coupling with A and B excitons. Strong interaction is sensitive to changes in the number of MoS_2 layers. We first examined the number of MoS_2 layers in the Au/MoS_2 heterostructure by Raman spectrum, as shown in Fig. 1(c). As the number of

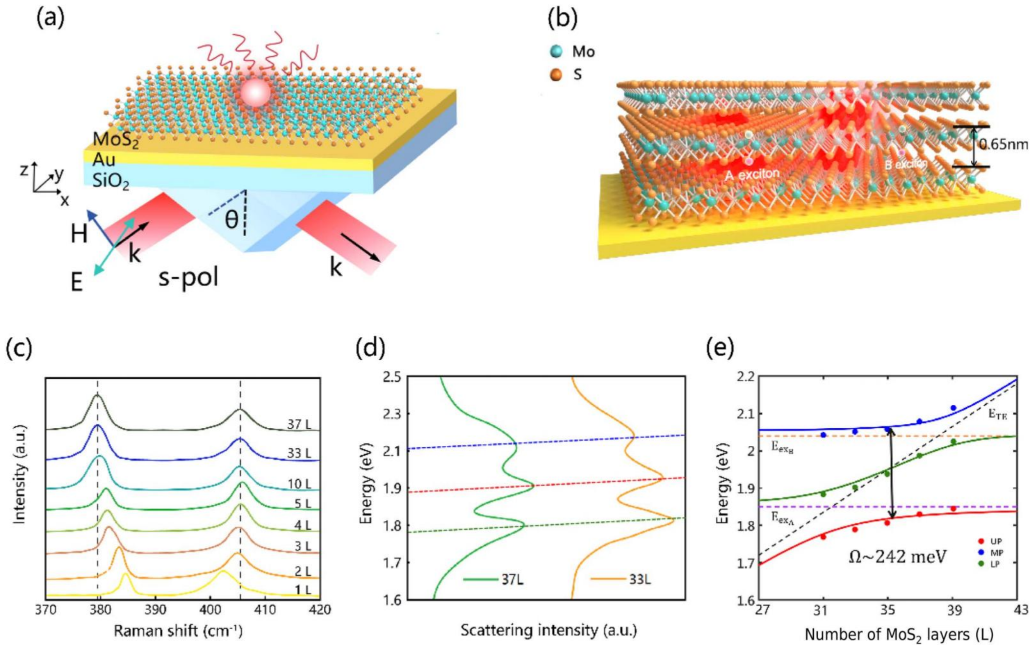

Fig. 1. (a) Schematic showing the excitation of TE waves in an Au/MoS$_2$ heterostructure by using s-polarized light and the extraction of scattering spectra by using a PS nanosphere. (b) Schematic showing the TE wave strong coupling with the A- and B- excitons in MoS$_2$; its variation is sensitive to the number of layers in MoS$_2$. (c) Raman spectra of MoS$_2$ samples with different numbers of layers (1–5, 10, 33, and 37 layers). (d) Strong coupling scattering spectra of 33- and 37-layer MoS$_2$ samples. (e) UP, MP, and LP branches (solid symbols) extracted from the scattering spectra.

MoS$_2$ layers gradually increases from one to five, the two characteristic peaks of MoS$_2$ in the Raman spectra can be clearly seen as they gradually shift towards 379 cm^{-1} and 407 cm^{-1}. When the number of MoS$_2$ layers reaches five and continues to increase, the shifts of the two characteristic peaks of MoS$_2$ become unrecognizable due to the weakening of the shearing and compression modes. The right peak stabilizes at 407 cm^{-1}, and the left peak also stabilizes and remains at 379 cm^{-1} when the number of layers continues to increase to 10. It can be observed that the two characteristic peaks in the Raman spectra of MoS$_2$ for layers 33 and 37 almost completely overlap at 379 cm^{-1} and 407 cm^{-1}. In Fig. 1(d), we show the strong coupling scattering spectra of Au/MoS$_2$ heterostructures with 33 and 37 layers of MoS$_2$, respectively. The TE wave excited in the Au/MoS$_2$ heterostructures interacts with the A- and B-excitons in the MoS$_2$ entering the strong coupling interval. The scattering spectrum shows a double Rabi splitting due to strong coupling, with three clearly identifiable Rabi splitting peaks. The shift in the strong coupling spectra is sensitive to the number of MoS$_2$ layers, with the Rabi splitting peak in the strong coupling spectra redshifted by 4 nm for two additional layers of MoS$_2$ (i.e., a 1.3 nm increase in thickness). Meanwhile, by adjusting the number of MoS$_2$ layers in the Au/MoS$_2$ heterostructure, the system can be tuned to strong coupling regime. The Rabi splitting of about 242 meV is obtained by fitting the three-resonator coupling model, as shown in Fig. 1(e).

In general, the SPPs supported by the surface of a metal film (or the metal–air interface) are TM waves, which can only be excited by p-polarized light, with the longitudinal electric field (E_x) generated by the collective oscillation of free electrons on the metal surface. However, TE waves cannot establish the same propagating electric field on the surface of a thin metal film, and no analytical solution exists for its corresponding Maxwell's equations. It has been demonstrated that propagatable TE waves can be established by covering a metal film with a high refractive index dielectric layer of a certain thickness. Utilizing the mirror effect of metal nanofilms, magnetic dipoles (MDs) in metal–TMDC heterostructures can be established from electric dipoles (EDs) excited in TMDCs. By further expanding the transverse dimensions of the TMDCs, periodically aligned MDs can be generated in the heterostructures, thus establishing a TE wave with one electric field component (E_y) and two magnetic field components (H_x and H_z). This results in the formation of a strong localized electric field in the MoS$_2$ layer; when the optical thickness of the TMDCs exceeds a critical value, the TE wave resonance supported by the Au/MoS$_2$ heterostructure is located in the visible spectrum where an analytical solution to the set of Maxwell's equations for the TE wave exists (see Appendix A).

To further investigate the physical properties of TE waves that are deeply involved in strong coupling processes, we selected an Au/MoS$_2$ heterostructure with appropriate thickness and excited at an incident angle of 46° as the numerical simulation model. Under these structural parameters and incident angle, the resonance position of the TE wave in the Au/MoS$_2$ heterostructure coincides with the wavelength of the MoS$_2$ exciton. In Figs. 2(a) and 2(b), we have calculated the electromagnetic field distribution in the Au/MoS$_2$ heterostructures under s-polarized light excitation along the y-axis direction ($h_{\mathrm{Au}} = 50$ nm, $h_{\mathrm{MoS_2}} = 25$ nm, $\theta = 46°$) using numerical simulation. The red dashed line represents the bottom of

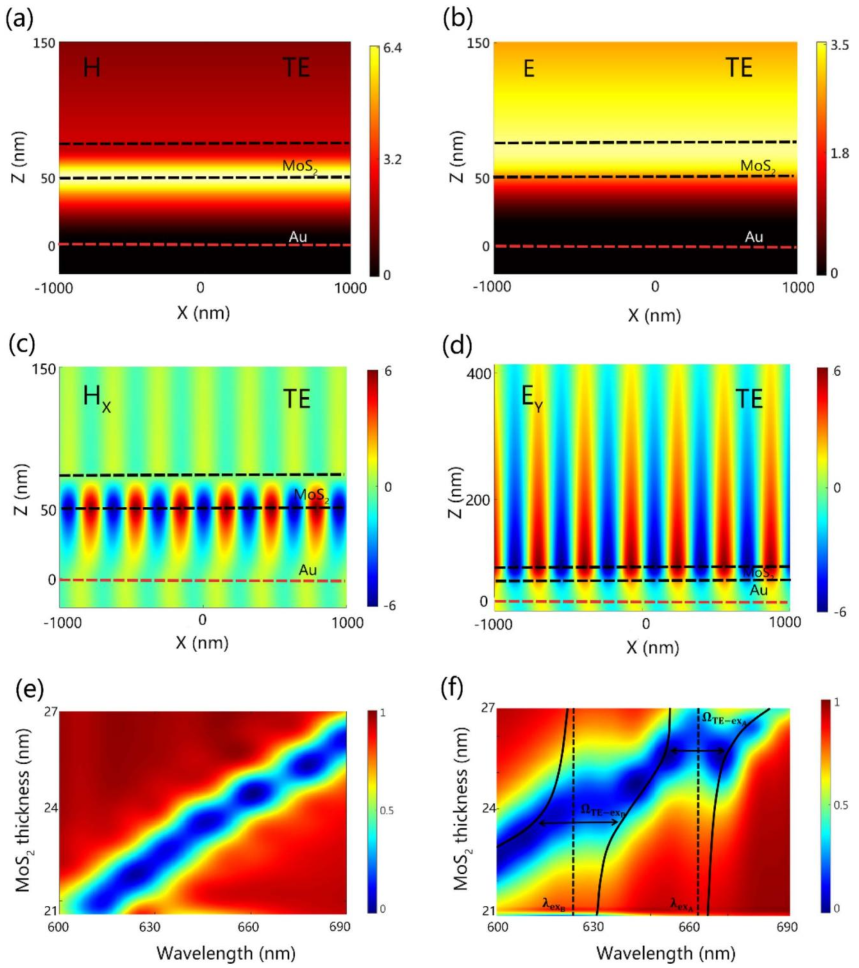

Fig. 2. (a) Total magnetic field and (b) electric field distribution in the XZ plane calculated for the TE wave in the Au/MoS$_2$ heterostructure ($h_{\mathrm{Au}} = 50$ nm, $h_{\mathrm{MoS}_2} = 25$ nm, $\theta = 46°$). (c) H_x component and (d) E_y component of TE wave. Dependence of the resonant wavelength of the TE wave on the thickness of MoS$_2$ calculated for the Au/MoS$_2$ heterostructure with $\theta = 46°$ with MoS$_2$ excitons switched off (e) and on (f).

the Au nanofilm, and the two black dashed lines represent the height of MoS$_2$ on the Au nanofilm. It has been demonstrated that the TE wave supported by Au/MoS$_2$ heterostructures exhibits the characteristic of electromagnetic field spatial separation. The magnetic field of the TE wave is predominantly localized at the interface between the Au film and MoS$_2$, whereas the electric field of the TE wave is strongly localized within the MoS$_2$ layer. This greatly minimizes the propagation loss due to the collective oscillation of the electrons in the metal film, thereby enhancing the Q factor and narrowing the linewidth of the TE wave. In Fig. 2(c) the TE wave forms a horizontally oriented magnetic standing wave (H_x) at the interface between the Au film and MoS$_2$ during propagation, while Fig. 2(d) indicates the existence of a standing wave (E_y) in the MoS$_2$ layer, which results in the formation of a strong localized electric field in the MoS$_2$ layer, which confirms the theory we presented above. Therefore, the TE wave supported by Au/MoS$_2$ heterostructures has a stronger local electric field and lower damping rate. This allows the TE wave to be utilized to generate a stronger interaction with the excitons of MoS$_2$.

The TE wave resonance supported by the Au/MoS$_2$ heterostructures varies with the incidence angle. By turning off the two excitons of MoS$_2$, we have demonstrated the 2D reflectance spectra of the Au/MoS$_2$ heterostructures at different incidence angles through numerical simulations. A change in incidence angle of about 15° is sufficient to make the TE wave resonance shift across the entire visible spectral region. We switched on two excitons of MoS$_2$ located at 625 and 670 nm to observe the strong coupling behavior of the Au/MoS$_2$ heterostructures. When focusing on the wavelength of 600–700 nm, we observe the anticrossing behaviors of the reflection spectrum at the two exciton wavelengths of MoS$_2$, which implies the existence of exciton–photon strong coupling (see Appendix B). The exciton–photon coupling in the Au/MoS$_2$ heterostructure can be described using the coupled harmonic oscillator model. Its corresponding Hamiltonian with three eigenvalues can be expressed as

$$\hat{H} = \begin{pmatrix} E_{\mathrm{TE}} - \frac{j\hbar\gamma_{\mathrm{TE}}}{2} & g_{\mathrm{TE-ex_A}} & g_{\mathrm{TE-ex_B}} \\ g_{\mathrm{TE-ex_A}} & E_{\mathrm{A}} - \frac{j\hbar\gamma_{\mathrm{A}}}{2} & g_{\mathrm{ex_A-ex_B}} \\ g_{\mathrm{TE-ex_B}} & g_{\mathrm{ex_A-ex_B}} & E_{\mathrm{B}} - \frac{j\hbar\gamma_{\mathrm{B}}}{2} \end{pmatrix}. \tag{1}$$

Here E_{TE}, E_{A}, and E_{B} are the resonance energies of the uncoupled TE wave, A-exciton, and B-exciton. γ_{TE}, γ_{A}, and γ_{B} are the corresponding dissipation rates. Dissipation rates can be obtained from the reflection spectrum of TE waves and the PL spectrum of MoS_2, respectively (see Appendix C). g_{TE-ex_A}, g_{TE-ex_B}, and $g_{ex_A-ex_B}$ are the coupling strengths between the TE wave and the A-exciton, between the TE wave and the B-exciton, and between the A-exciton and the B-exciton. Since the resonance energies of the two excitons are far apart, we have $g_{ex_A-ex_B} = 0$. The Rabi splitting values extracted from the zero detuning energy of our strong coupling reflection spectra are $\Omega_{TE-ex_A} \approx 103.6$ meV and $\Omega_{TE-ex_A} \approx 105.9$ meV, both of which satisfy the strong coupling criterion of $\hbar\Omega_{TE-ex} > |\gamma_{TE} \pm \gamma_{ex}|/2$. This is an indication that our exciton–photon hybrid system has entered the strong coupling range. We can manipulate the coupling strength of the TE wave–exciton hybrid system by adjusting the angle of incidence.

Similarly, we observe that the thickness of MoS_2 in the Au/MoS_2 heterostructures affects the resonant peak position of the TE waves, while changes in the thickness of the Au film cause a broadening of the TE wave linewidth (see Appendix E). As shown in Fig. 2(e), we first switched off the MoS_2 excitons and fixed the angle of incidence at 46°. We then calculated the 2D reflectance spectra of Au/MoS_2 heterostructures with a series of thickness gradients of MoS_2, while keeping thickness of the Au film unchanged. Our results show that as the thickness of MoS_2 is gradually increased from 21 to 27 nm, the resonance of TE wave is gradually redshifted from 600 to 690 nm sweeping through the two excitons of MoS_2 at 625 and 670 nm. Similarly, we observe a significant double Rabi splitting at the two exciton leaps in MoS_2 in Fig. 2(f). The strong exciton–photon coupling in the Au/MoS_2 heterostructure is produced by the thickness change.

B. Experimental Measurement of Strong Coupling Spectra in the Au/MoS_2 Heterostructure

In the experiment, we used the K–R configuration shown in Fig. 3(a) to measure the strong coupling information of the Au/MoS_2 heterostructure. We added a polarizer to the excitation light source system to control the polarization state of the incident light and used an angle adjustment knob arm to control the incident angle of the excitation light source, with an accuracy of 0.5°. To experimentally verify the exciton–photon strong coupling arising in the Au/MoS_2 heterostructure, we use the reflection spectra at different incidence angles from 45.5° to 48° to extract the Rabi splitting. At this point, the resonant wavelength range of the TE wave coincides with the exciton state transition of MoS_2. Changes in the incident angle support energy exchange between the TE wave and the exciton during the resonant shift process, thereby achieving strong coupling. In experiments, we used collimated white light with a diameter of about 1.0 cm to excite TE waves in Au/MoS_2 heterostructures. The large area of Au nanofilms enabled us to continuously change the angle of incidence for measurements to find the optimal coupling strength. However, it was difficult to precisely focus the spot onto the small-sized MoS_2 in reflectance spectroscopy measurements. As an alternative, we introduce PS nanospheres (which have a low refractive index of about 1.5) with a diameter of about 350 nm above the Au/MoS_2 heterostructure, which can be used as a scattering

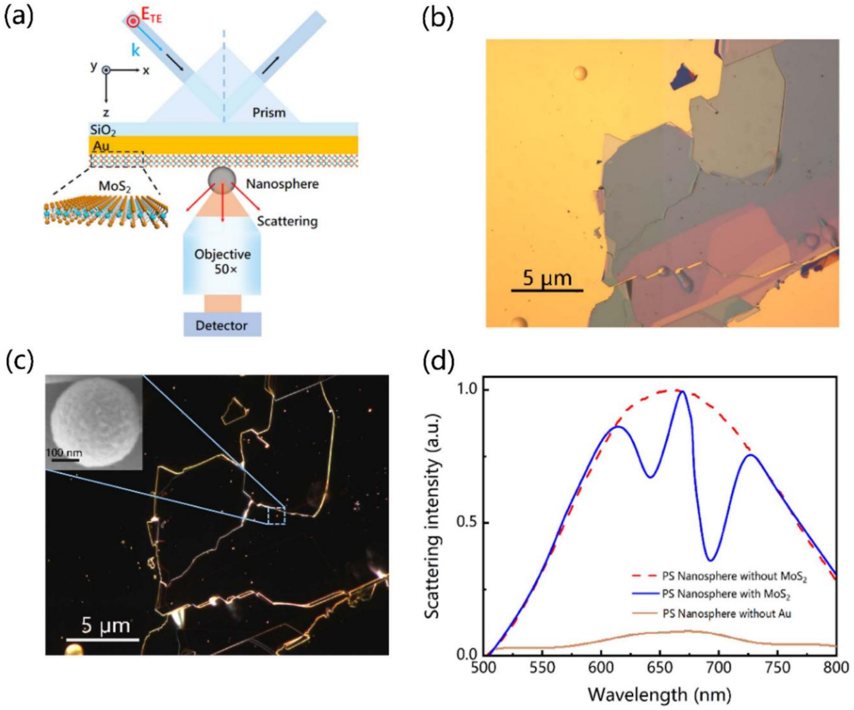

Fig. 3. (a) Schematic showing the excitation of TE waves in the Au/MoS_2 heterostructure by s-polarized light incident K–R configuration [64] and the extraction of TE waves using PS nanospheres. (b) Microscope bright-field image of PS nanospheres placed on the MoS_2/Au heterostructure. (c) Microscope dark-field image of PS nanospheres placed on the MoS_2/Au heterostructure (inset is SEM image of PS nanosphere). (d) Experimentally measured scattering spectra of PS nanospheres on Au films with/without MoS_2 and PS nanospheres on MoS_2 without Au films.

antenna for the measurement of TE waves. The PS nanospheres have a broad scattering spectrum in the visible spectral range and do not have any optical resonance. In our experiments, we obtained multilayer MoS_2 using mechanical stripping method and transferred MoS_2 onto a SiO_2 substrate deposited with 50 nm Au nanofilms by the PDMS transfer method. We then dropped aqueous solution containing PS nanospheres on the surface of the Au/MoS_2 heterostructure and allowed it to dry naturally. In our experiments, we measure the forward scattering of PS nanospheres to extract strong coupling information. The experimental setup is shown in Fig. 3(a). The bright-field image of Fig. 3(b) demonstrates the experimentally prepared Au/MoS_2 heterostructure, and in the dark-field image of the microscope in Fig. 3(c) we can clearly observe the PS nanospheres randomly distributed on the surface of MoS_2. The inset shows the SEM image of the PS nanospheres. We simultaneously measured the scattering spectra of PS nanospheres on Au films and Au/MoS_2 heterostructures, as shown in Fig. 3(d). Rabi splitting in the scattering spectra is observed in the presence of MoS_2; the Rabi splitting in the spectra is caused by the strong coupling of the TE wave to the excitons in MoS_2. We also measured the scattering spectra of PS nanospheres on MoS_2 without Au films. The scattering intensity in the spectrum decreases significantly, and no Rabi splitting phenomenon is observed. This is because the absence of the Au film prevents TE waves from forming in the Au/MoS_2 heterostructure, while the high absorption rate of the multilayer MoS_2 causes most of the incident light to be strongly absorbed.

In Fig. 4(a), we show the angle-resolved scattering spectra measured in the Au/MoS_2 heterostructure. The Au/MoS_2 heterostructure used in the measurements has a MoS_2 thickness of 22.7 nm and an Au film thickness of 50 nm. When the angle of incidence is gradually increased from 45.5° to 48°, the scattering spectra at each angle can be observed at the positions of the two exciton states at 625 and 670 nm, with clear Rabi splitting, indicating strong exciton–photon coupling. Meanwhile, the detuning of the exciton–photon coupling system can be dynamically adjusted by the change of the incident angle. The strong coupling system in the Au/MoS_2 heterostructure reaches zero detuning state when the incident angle reaches 46.5°. In Fig. 4(b), we show the dependence of the energy of the three hybrid modes on the detuning energy among the TE wave, the A-exciton, and the B-exciton, while fitting the hybrid system with the coupled harmonic oscillator model mentioned above. The experimental measurements are in very good agreement with our theoretical predictions. Since the TE wave excited in the Au/MoS_2 heterostructure is characterized by low loss and a high Q factor, and because we directly use multilayer MoS_2 as the heterostructure constituent material instead of covering the TMDCs on top of the high refractive index dielectric layer, we achieved a stronger electric field localization effect in the upper layers of the heterostructure. As a result, we obtain an ultrahigh Rabi splitting of about 310 meV at the zero-detuned harmonic of the hybrid system. This value greatly exceeds the Rabi splitting of all previous double-resonance subsystems and is also the largest value of

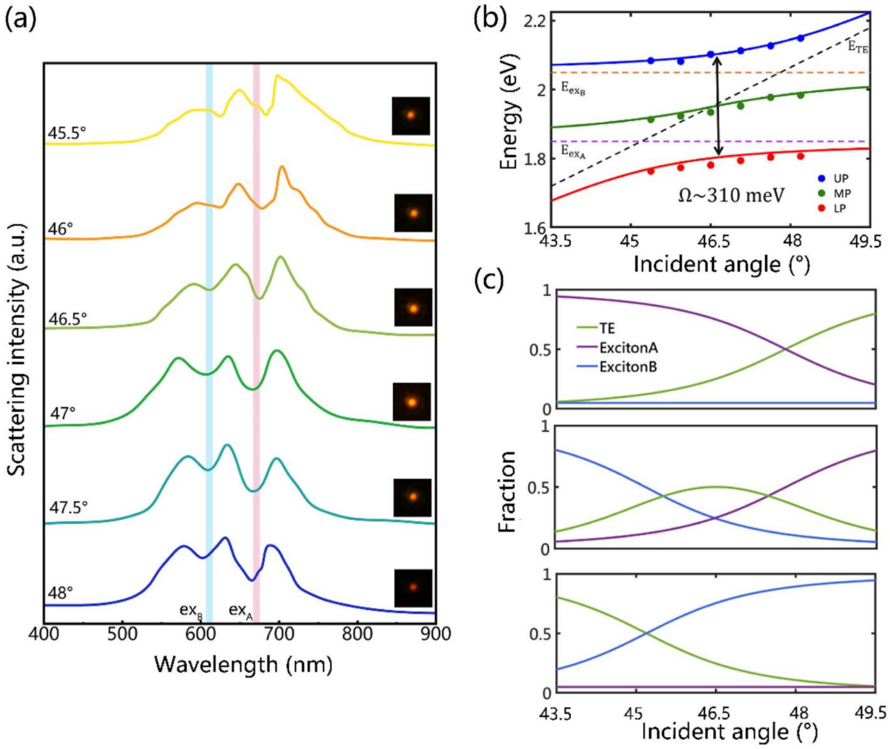

Fig. 4. (a) Experimentally measured scattering spectra of PS nanospheres placed on Au/MoS_2 heterostructures and excited with s-polarized light at different angles of incidence. CCD images of PS nanospheres are shown as insets. (b) Energy dependency of the hybrid modes on the energy detuning. The points are the experimental results, while the solid colored curves are the fitting results based on the coupled harmonic oscillator model. (c) Fraction of TE waves and two excitons (A-exciton and B-exciton) in the LP (top), MP (middle), and UP (bottom) branches of the hybrid modes.

Table 1. Comparison of Coupling Strengths of Different TMDC Materials Coupling Systems

2D Material	Mode	T	Rabi Splitting (meV)	Ref.
1 L WS_2	LSPR-Exciton	RT	106	[22]
1 L WS_2	LSPR-Exciton	6–300 K	120–150	[31]
1 L WSe_2	LSPR-Exciton	RT	83	[40]
1 L WS_2	LSPR-Exciton	RT	85	[60]
Multilayer WS_2	LSPR-Exciton	RT	100	[61]
Multilayer WSe_2	LSPR-Exciton	RT	137–144	[63]
Multilayer MoS_2	TM-Exciton	RT	81–93	[65]
1 L WS_2	TE-Exciton	RT	145	[66]
Multilayer MoS_2	TE-Exciton	RT	310	This work

coupling strength observed in a triple-resonance system under room-temperature air conditions reported to date (see Table 1). In Fig. 4(c), we calculate the percentages of excited TE waves, A- and B-excitons in each of the three polarizers branches in the Au/MoS_2 heterostructure. The results show that both A- and B-excitons have a nonnegligible contribution (25%) to the MP branch, suggesting that we have tuned the strong coupling system by a suitable incidence angle. This adjustment allows the TE waves with a suitable linewidth to successfully mediate the hybridization of A- and B-excitons in the multilayer MoS_2.

C. MoS_2 Layer Number Sensing Based on Strong Coupling Spectra

The effect of MoS_2 thickness on the strong coupling spectra in the Au/MoS_2 heterostructures allows us to accurately measure the number of MoS_2 layers by observing the shift in the strong coupling spectra. In our experiments, we prepared MoS_2 samples with 31, 33, 35, 37, and 39 layers, respectively, and transferred them to Au films, each with a thickness of 50 nm. Figure 5(a) shows the measured scattering spectrum obtained under the excitation of s-polarized light at an angle of incidence of 46°. In the scattering spectra of the Au/MoS_2 heterostructure with 31 layers of MoS_2, we observe Rabi splitting peaks due to strong exciton–photon coupling at about 570, 640, and 695 nm wavelengths, which are labeled as Peak 1, Peak 2, and Peak 3, respectively. The shift variations of the peaks are correspondingly indicated by red dashed, blue dashed, and pink dashed lines in Fig. 5(a). In accordance with theoretical predictions, the Rabi splitting peaks of the scattering spectra shift with the change of thickness of MoS_2. When the number of MoS_2 layers is gradually increased from 31 to 39, Peak 1 is redshifted from 570 to 586 nm, Peak 2 is redshifted from 640 to 657 nm, and Peak 3 is redshifted from 690 to 711 nm. The Rabi splitting peaks 1, 2, and 3 are redshifted by about 16 nm when MoS_2 is increased by eight layers. These shifts are clearly and accurately detected by our spectrometer. We extracted the wavelength values corresponding to the Rabi splitting peaks 1, 2, and 3 in the scattering spectra of each group of the Au/MoS_2 heterostructures and fitted them as shown in Fig. 5(b). The fitting results show that the Rabi splitting peaks in the strong coupling scattering spectra are linearly related to the change of the number of layers of MoS_2, i.e, for each increase of the thickness of MoS_2 (here we uniformly assume the thickness of one layer of MoS_2 to be 0.65 nm). The three Rabi splitting peaks in the strong coupling scattering spectra are redshifted by about 2 nm, and the spectrometer can easily and accurately capture this level of displacement in the experiment, which allows us to accurately identify the number of layers of MoS_2 by optical methods. In Fig. 5(c), we used AFM to measure the thickness of MoS_2 in samples 1–5 and measured the corresponding thicknesses of 20.2, 21.4, 22.7, 23.6, and 25.1 nm for the 31, 33, 35, 37, and 39 layers of MoS_2, respectively. The results of AFM are in high agreement with the results of our optical sensing approach. Meanwhile, we fit the experimental data using the coupled harmonic oscillator model and obtained a Rabi splitting of about 242 meV. The Rabi splitting line shape of the scattering spectrum changes with the thickness of MoS_2, demonstrating that detuning of the strong coupling system in the Au/MoS_2 heterostructure can be achieved by adjusting the thickness of MoS_2 (see Appendix F). The MoS_2 layer number sensing method based on the Rabi splitting peak displacement of strong coupling scattering spectra has high sensitivity and accuracy and malleability. The number of MoS_2 layers of 31–39 measured in the experiment is linearly related to the redshift of the Rabi splitting peak, so this measurement method can be extended to the detection of TMDCs in a larger range of layer numbers.

3. METHODS

A. Sample Preparation

The Au/MoS_2 heterostructures used in this paper were prepared by the following steps. First, an Au film with a thickness of 50 nm was deposited on a SiO_2 substrate by magnetron sputtering. Then, multilayers of MoS_2 were obtained by mechanical stripping, and MoS_2 was transferred onto the Au film by the PDMS transfer method. An aqueous solution containing PS nanospheres was dropped onto the Au/MoS_2 heterostructures and dried naturally. Measurement of MoS_2 thickness was done by AFM (Nano Wizard 4 Nanoscience, JPK Instruments AG).

B. Optical Characterization

The TE wave excited in the Au/MoS_2 heterostructure, as shown in Fig. 4(a), can be excited by the K–R configuration. A prism made of SiO_2 is placed on the sample and coated with silicone oil (the refractive index of silicone oil is close to that of SiO_2) between the sample and the prism. The s-polarized light is coupled into the Au/MoS_2 heterostructure using total internal reflection occurring on the surface of the prism. Scattering spectra of PS nanospheres placed on Au/MoS_2 heterostructures were collected by an inverted microscope (Axio Observer A1, Zeiss) configured with a color charge-coupled device (CCD, DS-Ri2, Zeiss) and a spectrometer (SR-500i-B1, Andor). A polarization analyzer was inserted in the collection channel to control the scattered light's polarization, and dark-field images were measured by a commercial optical microscope equipped with a standard dark-field illumination module (BX51, Olympus) using a 100× dark-field objective

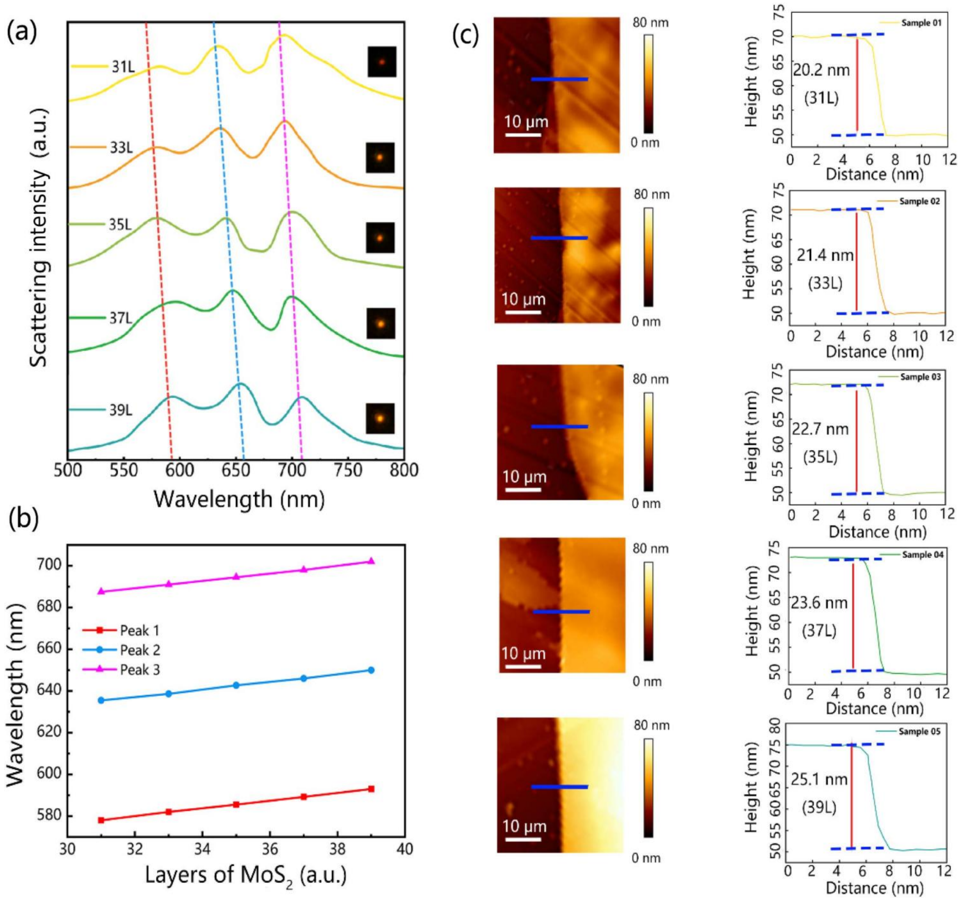

Fig. 5. (a) Experimentally measured scattering spectra of PS nanospheres excited by s-polarized light placed on Au/MoS$_2$ heterostructures with different thicknesses of MoS$_2$; CCD images of the scattered light are shown as insets (five samples in total, numbered Sample 1–Sample 5). (b) Layer-wavelength shift relation corresponding to the three Rabi splitting peaks extracted from the strong coupling scattering spectrum. (c) AFM images of Sample 1–Sample 5 (left column) and corresponding height distributions (right column).

(NA 0.8, MPLFLN, Olympus). Raman spectra of multilayered MoS$_2$ on Au nanofilms were acquired using a confocal Raman spectrometer (Renishaw InVia), using a 50× objective (NA 0.5, Germany 566036, Leica).

C. Numerical Simulation

The numerical simulations in this paper were conducted using the finite-difference time-domain (FDTD) technique (FDTD Solutions). In the numerical simulations, the dielectric constants of Au and MoS$_2$ were taken from the previous literature [67,68]. The thickness of each MoS$_2$ layer was set to 0.65 nm, the refractive index of the prism was set to 1.5, and the refractive index of the surrounding medium was set to 1.0. A mesh size as small as 0.2 nm was used in the gap region between the nanosphere and MoS$_2$ to ensure the convergence of the numerical simulations and the achievement of accurate results. Perfectly matched layer (PML) boundary conditions were used to terminate the finite simulation region.

4. CONCLUSION

In summary, we have realized TE surface waves with low loss and a high *Q* factor that can be excited by s-polarized light and stably propagate in metal-TMDC heterostructures by controlling the dimensions of the TMDCs and the spatial refractive index difference in the structure. Leveraging the high refractive index of the TMDCs, the electromagnetic field of the TE wave induces a special separation in the subwavelength thickness dimension, which lifts the strong local electric field into the TMDC layer, enabling strong coupling between the TE wave and the two excitons in the MoS$_2$, with a coupling strength significantly stronger than that of a typical system. In experimental studies employing PS nanospheres as scattering particles, we extracted the strong coupling scattering spectra between the TE waves and the two excitons, revealing the photon–exciton strong coupling through the angular and thickness-resolved scattering spectra. Further analysis of these scattering spectra confirmed the linear relationship between the displacement of strong coupling scattering spectra and the number of MoS$_2$ layers, allowing for accurate sensing of MoS$_2$ thickness, verified by AFM. Our findings not only open new avenues for manipulating strong light–matter interactions in TMDCs but also introduce a novel method for precisely characterizing the thickness of TMDCs.

APPENDIX A: REFLECTANCE SPECTRA OF Au/MoS₂ HETEROSTRUCTURES

In Fig. 6, we show the reflection spectra of the Au/MoS_2 heterostructure and the imaginary part of the MoS_2 dielectric constant corresponding to this thickness, obtained by numerical simulations for an Au film thickness of 50 nm, a MoS_2 thickness of 30 nm, and an incidence angle of 46°. We note that TE waves with suitable linewidths and resonant wavelengths can be obtained by properly tuning the structural parameters, thus realizing the strong coupling system in multilayer MoS_2.

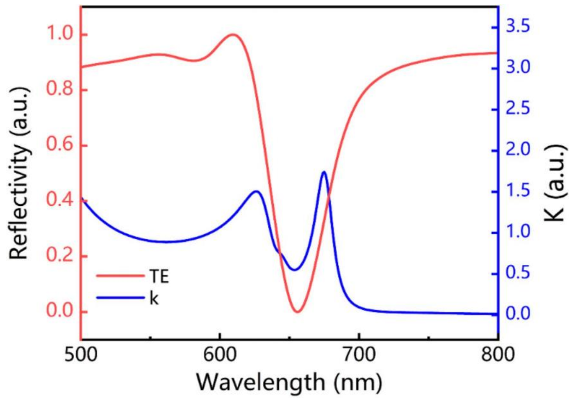

Fig. 6. Numerically simulated reflectance spectra of Au/MoS_2 heterostructures ($\theta = 46°$, $h_{Au} = 50$ nm, $h_{MoS_2} = 30$ nm) and the imaginary part of the dielectric constant of multilayer MoS_2.

APPENDIX B: ELECTRIC AND MAGNETIC FIELD COMPONENTS OF TE WAVE

As shown in Fig. 7(a), we calculated 2D reflectance spectra of the Au/MoS_2 heterostructures at different incidence angles and switched on two excitons of MoS_2 located at 625 and 670 nm, observing the strong coupling behavior of the Au/MoS_2 heterostructures in Fig. 7(b).

APPENDIX C: DISSIPATION RATES OF TE WAVES AND EXCITONS

In Fig. 8(a), we present the reflection spectrum of TE waves in the Au/MoS_2 heterostructure ($h_{Au} = 50$ nm, $h_{MoS_2} = 25$ nm, with MoS_2 excitons switched off) calculated by numerical simulation. The dissipation rate of TE waves can be obtained from the linewidth of the TE wave reflection peak as $\gamma_{TE} = 23.3$ meV. In Fig. 8(b), we measured the PL spectrum of MoS_2, and the dissipation rates of the A-exciton and B-exciton of MoS_2 can be obtained by extracting the linewidth of the corresponding exciton peaks in the PL spectrum, which are $\gamma_{exA} = 41$ meV and $\gamma_{exB} = 63$ meV.

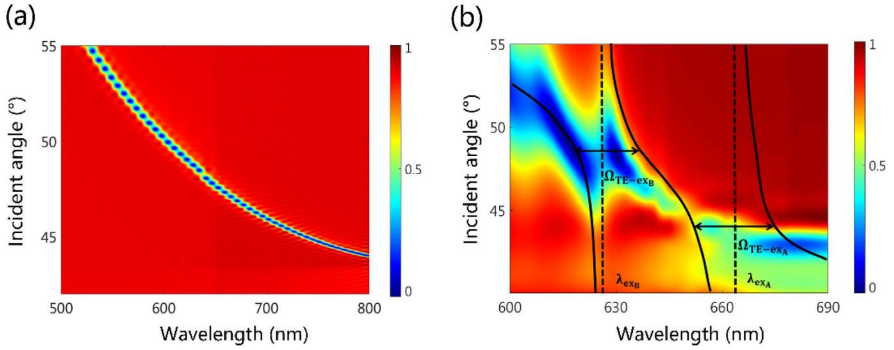

Fig. 7. Dependence of the resonant wavelength of the TE wave on the incidence angle of the excitation s-polarized light calculated for the Au/MoS_2 heterostructure with $h_{MoS_2} = 25$ nm with MoS_2 excitons switched off (a) and on (b).

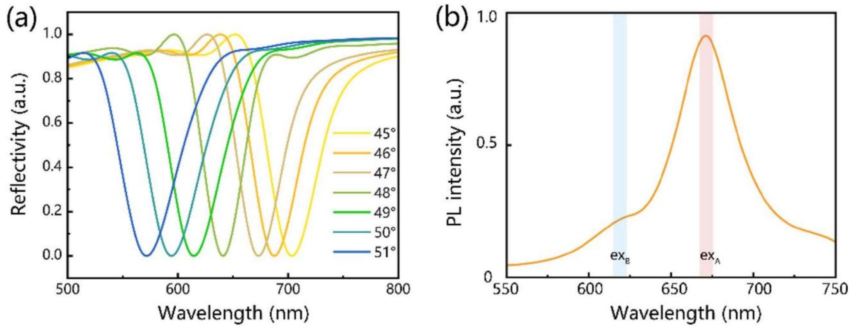

Fig. 8. (a) Reflection spectrum of TE waves in Au/MoS_2 heterostructures ($h_{Au} = 50$ nm, $h_{MoS_2} = 25$ nm, with MoS_2 excitons switched off). (b) PL spectrum of the MoS_2.

APPENDIX D: ANGLE-RESOLVED CHANGES IN THE TE WAVE ELECTRIC FIELD

In Fig. 9, we calculate the results of the E_y distribution in the XZ plane placed on the Au/MoS$_2$ heterostructure and excited using s-polarized light with different angles of incidence. Figures 9(a) and 9(b) show the calculated electric field distributions at $\theta = 45.5°$ and 46°; as the TE wave approaches the exciton resonance from the low-energy side, a weakening of the electric field and a broadening of the linewidth can be observed. Figures 9(c) and 9(d) show the calculated electric field distributions at $\theta = 47°$ and 48°. A significant electric field decay is observed as the TE wave propagates to the high-energy side of the exciton resonance, thereby indicating that the energy initially stored in the lower-branch TE wave has been transferred to the upper-branch MoS$_2$ exciton.

APPENDIX E: Au THICKNESS-RESOLVED DISPERSION DIAGRAMS OF Au/MoS$_2$ HETEROSTRUCTURES

We calculated the thickness-resolved dispersion diagrams of Au/MoS$_2$ heterostructures with different thicknesses of Au nanofilms as shown in Fig. 10(a) and reflectance spectra as shown in Fig. 10(b). It can be found that the thickness of the Au nanofilms affects the resonance of the TE wave excited in the Au/MoS$_2$ heterostructure to some extent and influences the linewidth of the TE wave to a larger extent. Therefore, we choose 50 nm Au nanofilms to construct Au/MoS$_2$ heterostructures with TE wave resonances that can cover the intervals of the two exciton leaps of MoS$_2$ and have suitable linewidths to realize the hybridization of A- and B- excitons in multilayer MoS$_2$.

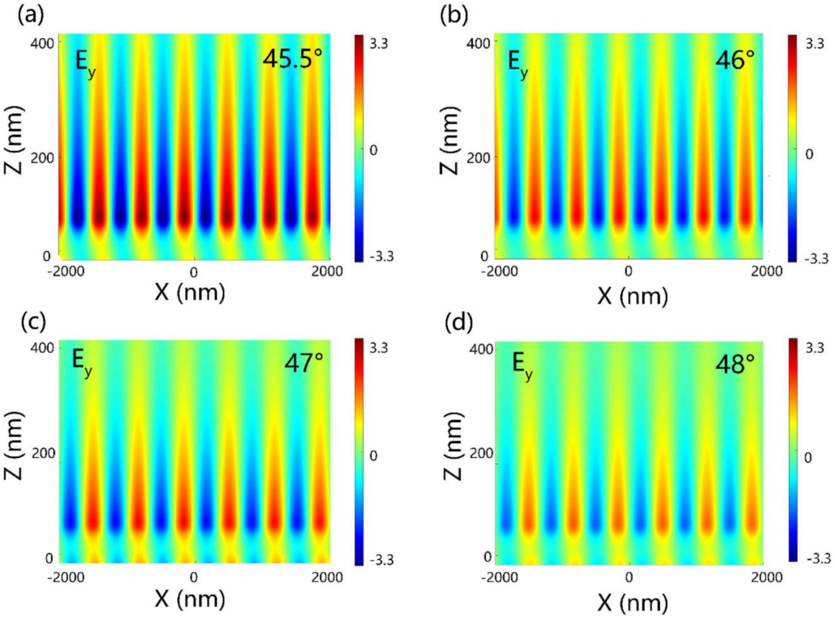

Fig. 9. Numerically simulated E_y electric field components of TE waves of Au/MoS$_2$ heterostructures excited at different incidence angles (a) 45.5°, (b) 46°, (c) 47°, and (d) 48°.

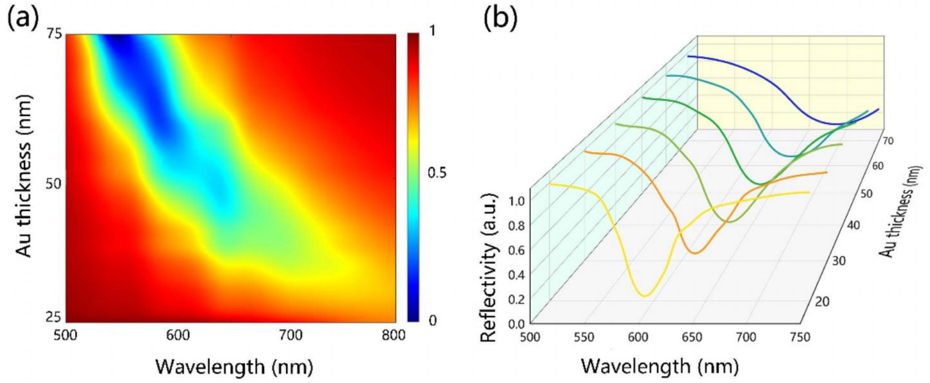

Fig. 10. (a) Thickness-resolved dispersion plots and (b) TE wave reflectance spectra of Au nanofilms in Au/MoS$_2$ heterostructures.

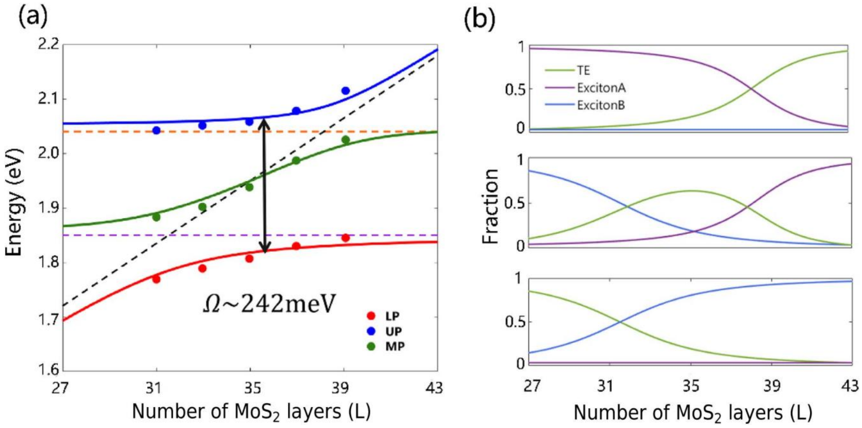

Fig. 11. (a) Energy dependency of the hybrid modes on the energy detuning as the MoS$_2$ thickness varies. The points are the experimental results, while the solid colored curves are the fitting results based on the coupled harmonic oscillator model. (b) Fraction of TE waves and two excitons (A-exciton and B-exciton) in the LP (top), MP (middle), and UP (bottom) branches of the hybrid modes.

APPENDIX F: STRONG COUPLING FITTING IN Au/MoS$_2$ HETEROSTRUCTURES AND COMPARISON OF THEIR COUPLING STRENGTHS

In Fig. 11(a), we used the coupled harmonic oscillator model to fit the scattering spectra of Au/MoS$_2$ heterostructures with different thicknesses of MoS$_2$ in Fig. 5(a) of the main text. A Rabi splitting of about 242 meV is obtained by fitting, demonstrating that the hybrid system based on MoS$_2$ thickness tuning has entered the strong coupling interval. Meanwhile, the TE waves excited in the Au/MoS$_2$ heterostructure and the percentage of A- and B-excitons in each of the three polarizer branches are plotted in Fig. 11(b), and both A- and B-excitons have non-negligible contributions to the MP branch, suggesting that we have modulated the strongly coupled system by changing the dimensions of the MoS$_2$ and made the TE waves with suitable linewidths successfully mediate the A- and B-excitons in the multilayer MoS$_2$ hybridization.

In Table 1, we summarize the strong photon–exciton coupling achieved in different monolayers and multilayers of TMDC materials combined with nanocavities or metal films reported in the literature. We observe Rabi splitting up to 310 meV in the Au/MoS$_2$ heterostructure system by adjusting the angle of incident light, which is the maximum value of the coupling strength observed in two-mode and three-mode systems at room temperature air conditions reported so far [22,31,40,60,61,63,65,66].

Funding. Natural Science Foundation of Guangdong Province (2025A1515012259); National Natural Science Foundation of China (12274148, 12374347, 12174123).

Disclosures. The authors declare no conflicts of interest.

Data Availability. The data and further information that support the findings of this study are available from the corresponding author upon reasonable request.

REFERENCES

1. Y. L. Li, A. Chernikov, X. Zhang, *et al.*, "Measurement of the optical dielectric function of monolayer transition-metal dichalcogenides: MoS$_2$, MoSe$_2$, WS$_2$, and WSe$_2$," Phys. Rev. B **90**, 205422 (2014).
2. S. Smolka, W. Wuester, F. Haupt, *et al.*, "Cavity quantum electrodynamics with many-body states of a two-dimensional electron gas," Science **346**, 332–335 (2014).
3. J. M. Raimond, M. Brune, and S. Haroche, "Colloquium: manipulating quantum entanglement with atoms and photons in a cavity," Rev. Mod. Phys. **73**, 565–582 (2001).
4. D. G. Baranov, M. Wersall, J. Cuadra, *et al.*, "Novel nanostructures and materials for strong light matter interactions," ACS Photonics **5**, 24–42 (2018).
5. E. Cao, W. H. Lin, M. T. Sun, *et al.*, "Exciton-plasmon coupling interactions: from principle to applications," Nanophotonics **7**, 145–167 (2018).
6. A. F. Kockum, A. Miranowicz, S. De Liberato, *et al.*, "Ultrastrong coupling between light and matter," Nat. Rev. Phys. **1**, 19–40 (2019).
7. G. Khitrova, H. M. Gibbs, M. Kira, *et al.*, "Vacuum Rabi splitting in semiconductors," Nat. Phys. **2**, 81–90 (2006).
8. T. Ming, L. Zhao, Z. Yang, *et al.*, "Strong polarization dependence of plasmon-enhanced fluorescence on single gold nanorods," Nano Lett. **9**, 3896–3903 (2009).
9. G. A. Wurtz, P. R. Evans, W. Hendren, *et al.*, "Molecular plasmonics with tunable exciton-plasmon coupling strength in J-aggregate hybridized Au nanorod assemblies," Nano Lett. **7**, 1297–1303 (2007).
10. S. Balci, C. Kocabas, S. Ates, *et al.*, "Tuning surface plasmon-exciton coupling via thickness dependent plasmon damping," Phys. Rev. B **86**, 235402 (2012).
11. L. H. Lin, M. S. Wang, X. L. Wei, *et al.*, "Photoswitchable Rabi splitting in hybrid plasmon-waveguide modes," Nano Lett. **16**, 7655–7663 (2016).
12. W. Chen, K. M. Beck, R. Bücker, *et al.*, "All-optical switch and transistor gated by one stored photon," Science **341**, 768–770 (2013).
13. T. Volz, A. Reinhard, M. Winger, *et al.*, "Ultrafast all-optical switching by single photons," Nat. Photonics **6**, 605–609 (2012).
14. P. Vasa, R. Pomraenke, G. Cirmi, *et al.*, "Ultrafast manipulation of strong coupling in metal-molecular aggregate hybrid nanostructures," ACS Nano **4**, 7559–7565 (2010).
15. Y. Ye, Z. J. Wong, X. F. Lu, *et al.*, "Monolayer excitonic laser," Nat. Photonics **9**, 733–737 (2015).
16. S. F. Wu, S. Buckley, J. R. Schaibley, *et al.*, "Monolayer semiconductor nanocavity lasers with ultralow thresholds," Nature **520**, 69–72 (2015).

17. S. K. Rajendran, M. J. Wei, H. Ohadi, *et al.*, "Low threshold polariton lasing from a solution-processed organic semiconductor in a planar microcavity," Adv. Opt. Mater. **7**, 1801791 (2019).
18. K. Hennessy, A. Badolato, M. Winger, *et al.*, "Quantum nature of a strongly coupled single quantum dot-cavity system," Nature **445**, 896–899 (2007).
19. H. Gross, J. M. Hamm, T. Tufarelli, *et al.*, "Near-field strong coupling of single quantum dots," Sci. Adv. **4**, eaar4906 (2018).
20. Q. P. Lu, Y. F. Yu, Q. L. Ma, *et al.*, "2D transition-metal-dichalcogenide-nanosheet-based composites for photocatalytic and electrocatalytic hydrogen evolution reactions," Adv. Mater. **28**, 1917–1933 (2016).
21. H. Wang, L. L. Yu, Y. H. Lee, *et al.*, "Integrated circuits based on bilayer MoS_2 transistors," Nano Lett. **12**, 4674-–4680 (2012).
22. J. X. Wen, H. Wang, W. L. Wang, *et al.*, "Room-temperature strong light-matter interaction with active control in single plasmonic nanorod coupled with two-dimensional atomic crystals," Nano Lett. **17**, 4689–4697 (2017).
23. S. Lepeshov, M. S. Wang, A. Krasnok, *et al.*, "Tunable resonance coupling in single Si nanoparticle-monolayer WS_2 structures," ACS Appl. Mater. Interfaces **10**, 16690–16697 (2018).
24. G. Y. Jia, Y. Liu, J. Y. Gong, *et al.*, "Excitonic quantum confinement modified optical conductivity of monolayer and few-layered MoS_2," J. Mater. Chem. C **4**, 8822–8828 (2016).
25. J. H. Sun, Y. J. Gu, D. Y. Lei, *et al.*, "Mechanistic understanding of excitation-correlated nonlinear optical properties in MoS_2 nanosheets and nanodots: the role of exciton resonance," ACS Photonics **3**, 2434–2444 (2016).
26. J. Liu, T. W. Lo, J. Sun, *et al.*, "A comprehensive comparison study on the vibrational and optical properties of CVD-grown and mechanically exfoliated few-layered WS_2," J. Mater. Chem. C **5**, 11239–11245 (2017).
27. T. Mueller and E. Malic, "Exciton physics and device application of two-dimensional transition metal dichalcogenide semiconductors," npj 2D Mater. Appl. **2**, 29 (2018).
28. A. Splendiani, L. Sun, Y. B. Zhang, *et al.*, "Emerging photoluminescence in monolayer MoS_2," Nano Lett. **10**, 1271–1275 (2010).
29. J. Fang, K. Yao, M. S. Wang, *et al.*, "Observation of room-temperature exciton-polariton emission from wide-ranging 2D semiconductors coupled with a broadband Mie resonator," Nano Lett. **23**, 9803–9810 (2023).
30. A. Boulesbaa, B. Huang, K. Wang, *et al.*, "Observation of two distinct negative trions in tungsten disulfide monolayers," Phys. Rev. B **92**, 115443 (2015).
31. A. Rose, J. R. Dunklin, H. Y. Zhang, *et al.*, "Plasmon-mediated coherent superposition of discrete excitons under strong exciton-plasmon coupling in few-layer MoS_2 at room temperature," ACS Photonics **7**, 1129–1134 (2020).
32. A. Canales, D. G. Baranov, T. J. Antosiewicz, *et al.*, "Abundance of cavity-free polaritonic states in resonant materials and nanostructures," J. Chem. Phys. **154**, 024701 (2021).
33. P. A. Thomas, K. S. Menghrajani, and W. L. Barnes, "Cavity-free ultrastrong light-matter coupling," J. Phys. Chem. Lett. **12**, 6914–6918 (2021).
34. R. Pandya, R. Y. S. Chen, Q. F. Gu, *et al.*, "Microcavity-like exciton-polaritons can be the primary photoexcitation in bare organic semiconductors," Nat. Commun. **12**, 6519 (2021).
35. I. Vurgaftman, B. S. Simpkins, A. D. Dunkelberger, *et al.*, "Comparative analysis of polaritons in bulk, dielectric slabs, and planar cavities with implications for cavity-modified reactivity," J. Chem. Phys. **156**, 034110 (2022).
36. B. Munkhbat, D. G. Baranov, M. Stührenberg, *et al.*, "Self-hybridized exciton-polaritons in multilayers of transition metal dichalcogenides for efficient light absorption," ACS Photonics **6**, 139–147 (2019).
37. Q. Wang, L. X. Sun, B. Zhang, *et al.*, "Direct observation of strong light-exciton coupling in thin WS_2 flakes," Opt. Express **24**, 7151–7157 (2016).
38. A. Canales, O. Kotov, and T. O. Shegai, "Perfect absorption and strong coupling in supported MoS_2 multilayers," ACS Nano **17**, 3401–3411 (2023).
39. Q. H. Wang, K. Kalantar-Zadeh, A. Kis, *et al.*, "Electronics and optoelectronics of two-dimensional transition metal dichalcogenides," Nat. Nanotechnol. **7**, 699–712 (2012).
40. M. E. Kleemann, R. Chikkaraddy, E. M. Alexeev, *et al.*, "Strong-coupling of WSe_2 in ultra-compact plasmonic nanocavities at room temperature," Nat. Commun. **8**, 1296 (2017).
41. G. Wang, A. Chernikov, M. M. Glazov, *et al.*, "Colloquium: excitons in atomically thin transition metal dichalcogenides," Rev. Mod. Phys. **90**, 021001 (2018).
42. W. S. Fang, L. Huang, S. Zaman, *et al.*, "Recent progress on two-dimensional electrocatalysis," Chem. Res. Chin. Univ. **36**, 611–621 (2020).
43. Y. Koo, T. Moon, M. Kang, *et al.*, "Dynamical control of nanoscale light-matter interactions in low-dimensional quantum materials," Light Sci. Appl. **13**, 18 (2024).
44. L. Wehmeier, S. J. Yu, X. Z. Chen, *et al.*, "Tunable phonon polariton hybridization in a van der Waals hetero-bicrystal," Adv. Mater. **36**, 2401349 (2024).
45. R. J. Shiue, X. T. Gan, Y. D. Gao, *et al.*, "Enhanced photodetection in graphene-integrated photonic crystal cavity," Appl. Phys. Lett. **103**, 241109 (2013).
46. S. Das, D. Huang, I. A. Verzhbitskiy, *et al.*, "Electrical control of valley polarized charged exciton species in monolayer WS_2," ACS Nano **18**, 30805–30815 (2024).
47. D. Xiao, G. B. Liu, W. X. Feng, *et al.*, "Coupled spin and valley physics in monolayers of MoS_2 and other group-VI dichalcogenides," Phys. Rev. Lett. **108**, 196802 (2012).
48. K. F. Mak, K. L. He, J. Shan, *et al.*, "Control of valley polarization in monolayer MoS_2 by optical helicity," Nat. Nanotechnol. **7**, 494–498 (2012).
49. H. L. Zeng, J. F. Dai, W. Yao, *et al.*, "Valley polarization in MoS_2 monolayers by optical pumping," Nat. Nanotechnol. **7**, 490–493 (2012).
50. T. Yu and M. W. Wu, "Valley depolarization due to intervalley and intravalley electron-hole exchange interactions in monolayer MoS_2," Phys. Rev. B **89**, 205303 (2014).
51. T. Yu and M. W. Wu, "Valley depolarization dynamics and valley Hall effect of excitons in monolayer and bilayer MoS_2," Phys. Rev. B **93**, 045414 (2016).
52. A. Ciattoni, A. Marini, C. Rizza, *et al.*, "Phase-matching-free parametric oscillators based on two-dimensional semiconductors," Light Sci. Appl. **7**, 5 (2018).
53. M. Zhao, Z. L. Ye, R. Suzuki, *et al.*, "Atomically phase-matched second-harmonic generation in a 2D crystal," Light Sci. Appl. **5**, e16131 (2016).
54. P. Y. Wu, W. Q. Lee, C. H. Liu, *et al.*, "Coherent control of enhanced second-harmonic generation in a plasmonic nanocircuit using a transition metal dichalcogenide monolayer," Nat. Commun. **15**, 1855 (2024).
55. G. Zograf, A. Y. Polyakov, M. Bancerek, *et al.*, "Combining ultrahigh index with exceptional nonlinearity in resonant transition metal dichalcogenide nanodisks," Nat. Photonics **18**, 751–757 (2024).
56. X. L. Li, W. P. Han, J. B. Wu, *et al.*, "Layer-number dependent optical properties of 2D materials and their application for thickness determination," Adv. Funct. Mater. **27**, 1604468 (2017).
57. M. A. Kats, R. Blanchard, P. Genevet, *et al.*, "Nanometre optical coatings based on strong interference effects in highly absorbing media," Nat. Mater. **12**, 20–24 (2013).
58. X. Zhang, Q. H. Tan, J. B. Wu, *et al.*, "Review on the Raman spectroscopy of different types of layered materials," Nanoscale **8**, 6435–6450 (2016).
59. M. Boukhicha, M. Calandra, M. A. Measson, *et al.*, "Anharmonic phonons in few-layer MoS_2: Raman spectroscopy of ultralow energy compression and shear modes," Phys. Rev. B **87**, 195316 (2013).
60. M. Stuhrenberg, B. Munkhbat, D. G. Baranov, *et al.*, "Strong light-matter coupling between plasmons in individual gold bi-pyramids and excitons in mono- and multilayer WSe_2," Nano Lett. **18**, 5938–5945 (2018).
61. J. Fang, S. C. Huang, K. Yao, *et al.*, "Tunable couplings of photons with bright and dark excitons in monolayer semiconductors on plasmonic-nanosphere-on-mirror cavities," J. Phys. Chem. C **127**, 9105–9112 (2023).
62. G. T. Papadakis, A. Davoyan, P. Yeh, *et al.*, "Mimicking surface polaritons for unpolarized light with high-permittivity materials," Phys. Rev. Mater. **3**, 015202 (2019).

63. S. L. Li, L. D. Zhou, F. Deng, *et al.*, "Transverse-electric-polarized polaritons propagating in a $WS_2/Si_3N_4/Ag$ heterostructure," Laser Photon. Rev. **16**, 100457 (2022).
64. E. Kretschmann and H. Raether, "Notizen: radiative decay of non radiative surface plasmons excited by light," Z. Für Naturforschung A **23**, 2135–2136 (1968).
65. J. Cuadra, D. G. Baranov, M. Wersäll, *et al.*, "Observation of tunable charged exciton polaritons in hybrid monolayer WS_2-plasmonic nanoantenna system," Nano Lett. **18**, 1777–1785 (2018).
66. S. J. Wang, L. V. Quynh, F. Vaianella, *et al.*, "Limits to strong coupling of excitons in multilayer WS_2 with collective plasmonic resonances," ACS Photonics **6**, 286–293 (2019).
67. P. B. Johnson and R. W. Christy, "Optical constants of the noble metals," Phys. Rev. B **6**, 4370–4379 (1972).
68. B. Munkhbat, P. Wróbel, T. J. Antosiewicz, *et al.*, "Optical constants of several multilayer transition metal dichalcogenides measured by spectroscopic ellipsometry in the 300–1700 nm range: high index, anisotropy, and hyperbolicity," ACS Photonics **10**, 2398–2407 (2022).